Contents list available at CBIORE journal website

International Journal of Renewable Energy Development

Journal homepage: https://ijred.cbiore.id

Research Article

Achieving superior tartrazine-tetracycline removal and hydrogen production with WO_3/g-C_3N_4/TiNTAs through integrated photocatalysis-electrocoagulation

Saddam Husein[a], Abdul Hamid Budiman[b], Eniya Listiani Dewi[c], Slamet[a*]

[a] *Department of Chemical Engineering, Faculty of Engineering, Universitas Indonesia, Depok 16424, Indonesia*

[b] *Research Center for Energy Conversion and Conservation, National Research and Innovation Agency (BRIN), South Tangerang 15314, Indonesia*

[c] *General Directorate of New Renewable Energy and Energy Conservation, Ministry of Energy and Mineral Resources, Jakarta, 10320, Indonesia*

Abstract. The study aims to evaluate the removal of tartrazine (TZ), tetracycline (TC), and a combination of both TZ+TC and hydrogen (H_2) production simultaneously using WO_3/g-C_3N_4/TiNTAs (W-CN-TiNT) nanocomposites. The processes used in this study were Electrocoagulation (EC), photocatalysis (PC), and a combination of photocatalysis-electrocoagulation (PC-EC) simultaneously. The synthesis of W-CN-TiNT nanocomposites was carried out using the in-situ Anodization (IA) method, which was then tested for its performance in the PC and PC-EC processes. The nanomaterials were characterized by various techniques such as X-ray diffraction (XRD), ultraviolet-visible diffuse reflectance spectroscopy (UV-Vis DRS), field emission scanning electron microscopy with energy dispersive X-ray spectroscopy (FESEM-EDX), high-resolution transmission electron microscopy with selected area electron diffraction (HRTEM-SAED), X-ray photoelectron spectroscopy (XPS), and photocurrent measurements. In the PC process, liquid chromatography-high-resolution mass spectrometry (LC-HRMS), UV-Vis spectrophotometer, and gas chromatography (GC) were used to assess the efficiency of pollutant removal and H_2 production. The results show that TZ is removed more easily than TC during the PC process, and the pollutant removal rate is correlated with H_2 production. This observation also applies to the EC process and the PC-EC. The PC-EC process is superior to the single process of removing the TZ+TC pollutants. The proposed approach has proven to be effective for TZ+TC removal and in enhancing H_2 production. The use of W-CN-TiNT nanocomposite as a photocatalyst is revolutionary. It significantly improves the process efficiency. This research provides a sustainable alternative solution that is environmentally friendly and can be applied for the treatment of pharmaceutical industrial wastewater containing complex organic compounds.

Keywords: Tartrazine, Tetracycline, Hydrogen Production, Photocatalysis, Electrocoagulation

Received: 27th Feb 2025; Revised: 8th April 2025 ; Accepted: 20th April 2025; Available online: 3rd May 2025

1. Introduction

Pharmaceutical waste from hospitals or the pharmaceutical industry often contains hazardous substances such as antibiotics and dyes (Husein *et al.,* 2023). Antibiotics such as TC can cause environmental contamination if not handled properly. TC has been detected in several aquatic environments, and its concentration reaches a maximum of 10 ng/L (Di Silvestre *et al.*, 2018). In addition to TC, dyes such as TZ can threaten the environment and human health. Thus, research on the decomposition of pharmaceutical waste with these two chemicals remains very limited. Until now, research efforts have mostly focused on waste containing hazardous substances (Bhamare, 2022). Effective pharmaceutical waste treatment is urgently needed to reduce environmental and human health risks. Aside from the above problems, the demand for renewable energy in the world is increasing, especially H_2, where H_2 can be a promising alternative energy source. To overcome this problem, it is necessary to develop a more cost-effective and environmentally friendly H_2 production process to reduce dependence on fossil-based energy sources (Eidsvåg *et al.*, 2021).

PC and EC are two processes used to manage pharmaceutical waste while producing renewable energy. The PC process utilizes photon energy, specifically sunlight, to help remove hazardous compounds, such as pharmaceutical waste and dyes while reducing the production of H_2 gas (Ji *et al.*, 2021; Nakata & Fujishima, 2012; Schneider *et al.*, 2014). Meanwhile, EC is an electrochemical process that removes pollutants from the air. The EC process has been described in detail by previous researchers (Emamjomeh & Sivakumar, 2009; Kabdaşlı *et al.*, 2012; Linares-Hernández *et al.*, 2009; Mollah *et al.*, 2001; Ouaissa *et al.*, 2014). In addition, integration of methodologies has been studied to improve efficiency in waste treatment and energy generation (Pelawi *et al.*, 2020; Sharfan *et al.*, 2018; Slamet & Kurniawan, 2018; Suárez-Escobar *et al.*, 2016). Hence, this study aims to produce a new method related to pharmaceutical pollutants treatment using the PC process with W-CN-TiNT nanocomposites synthesized through the IA method, which is rarely documented in the literature, unlike

* Corresponding author
Email: slamet@che.ui.ac.id (Slamet)

https://doi.org/10.61435/ijred.2025.61167
ISSN: 2252-4940/© 2025.The Author(s). Published by CBIORE

common synthesis methods such as PVD or SILAR, which often require higher temperatures and/or toxic chemical compounds (Güzeldir, Sağlam, and Ateş 2010).

The IA method allows the formation of oxide layers directly on the substrate surface or nanostructures that control the formation of morphology and composition (Shalom *et al*. 2014). This advantage is essential to enhance complete material-substrate integration, as well as improve overall stability, combined with an environmentally friendly synthesis procedure. Furthermore, the IA method facilitates morphological modification along with structural modification of nanomaterials, which occurs through the adjustment of certain electrochemical parameters. Thus, the IA method is a more flexible and encouraging tactic to enhance photocatalytic applications. Furthermore, this study uniquely showcases the performance of W-CN-TiNT nanocomposites synthesized by the IA method in the PC-EC process. The combination of PC-EC has rarely been explored before. In considering pollutants, this study discusses the handling of complex pharmaceutical industry pollutants, such as pollutants containing a mixture of TZ and TC.

Based on the description above, this study aims to investigate the effectiveness of W-CN-TiNT nanocomposites synthesized using the IA method in removing TZ and TC pollutants and producing H_2 through a combination of PC-EC processes. In addition to PC-EC, single PC and single EC processes were also carried out to transmit their effectiveness in removing TZ and TC pollutants and H_2 production.

2. Experimental Methods

2.1 Synthesis of WO_3/g-C_3N_4/TiNTAs Nanocomposite

The chemicals employed were analytical reagents sourced from Sigma Aldrich. A titanium plate size was 8 x 4 x 0.01 cm (Shaanxi Yunzhong Metal Technology Co., LTD, China). It was subjected to mechanical polishing using CW 1500 sandpaper. The titanium plate was thereafter submerged in a chemical solution of 40% HF (Merck), 65% HNO_3, and distilled water in a volume ratio of 1:3:46 for one minute. Afterward, it was cleansed with distilled water and subjected to sonication for 5 minutes to eliminate any residual contaminants.

W-CN-TiNT nanocomposites were synthesized using the IA method. This process was carried out in an electrolyte solution containing 98% glycerol, 0.5 wt% NH_4F, and 25 vol% water. A platinum plate acts as a cathode, and a titanium plate as an anode. Melamine and sodium tungstate dihydrate ($Na_2WO_4{\cdot}2H_2O$) were added to the electrolyte solution as precursors to synthesize W-CN-TiNT nanocomposites where 0.3 g of melamine was used as a precursor of g-C_3N_4 and 0.78 g of $Na_2WO_4{\cdot}2H_2O$ was used as a precursor of WO_3. The anodization process was conducted at a voltage of 50 V for 2 hours. After that, the sample was dried at room temperature for 30 minutes. The sample was then annealed in a furnace at a temperature of 550°C for 3 hours. This process was carried out at a heating rate of about 3°C/min to obtain the desired crystalline phase in the nanocomposite.

2.2 Characterizations of WO_3/g-C_3N_4/TiNTAs Nanocomposite

The characteristics of the nanocomposites were evaluated using characterization methods such as FESEM-EDX, HRTEM-SAED, XRD, UV-Vis DRS, XPS, photocurrent, and LC-HRMS. FESEM-EDX was employed to examine the surface morphology of the photocatalyst as well as to ascertain the exact physical parameters, such as nanotube dimensions, thickness, material composition, and distribution of catalytic constituents. The investigations were carried out at a voltage of 30 kV. This voltage was increased during the investigations. The average diameter of the nanotubes was evaluated through the Gaussian curve fitting technique, while the average length and thickness were measured through the instrument's built-in software.

The nanostructural characteristics were subsequently examined using HRTEM (FEI Tecnai G2 20 S-TWIN) with 200 kV supplemented by SAED analysis. The crystallographic characteristics of the nanocomposite were analyzed using XRD. It employed an Empyrean Series 3 Panalytical apparatus, which utilized a copper anode tube (λ = 0.15406 nm). XRD measurements were performed at 40 kV and 30 mA with a scan range of 10 to 60° in 2θ. The step size was 0.013°, and the scan step duration was 37.995 s. The crystallite size was determined using Scherrer equation relying on the full width at half maximum (FWHM) values of the XRD peaks

The optical characteristics and band gap energies were assessed using the Kubelka-Munk function. It was based on UV-Vis DRS within the wavelength range of 300–500 nm with an Agilent Cary 60 UV-Vis Spectrophotometer. An XPS examination was conducted using Shimadzu Axis Supra+ equipment to clarify the chemical states and surface composition of the nanocomposite.

2.3 Test for the Hydrogen Production and Tartrazine-Tetracycline Removal

The process of PC, EC, and PC-EC helped the formation of H_2 and the removal of TZ and TC pollutants. This method was carried out in an acrylic reactor containing one hybrid PC-EC device. The reactor contained 500 mL of TZ and TC solution with a concentration of 10 ppm, pH of 5, and added 0.2 g/L NaCl. The PC process test used W-CN-TiNT nanocomposite as a photocatalyst irradiated by two 250 W mercury lamps with a ratio of 17.25% UV light and 82.75% visible light.

The EC method used an aluminum plate as the anode and a stainless steel-316 plate as the cathode with a thickness of 1 mm and 2 mm, respectively. Each electrode had the same size at 8 cm x 4 cm, and the distance between the electrodes was 3 cm. The electrodes were connected to a power source with a voltage of 5 volts. The reactor in the PC-EC combination was separated between the PC and EC rooms by a micro-sized cloth partition. This partition was used to prevent the entry of $Al(OH)_3$ coagulant from the EC room to the PC room. As an initial step, the solution in the reactor flowed with argon gas for 5 minutes before testing, and this was done to remove oxygen from the mechanism. The specific parameters used in this PC-EC combination process were the specific and optimal result parameters obtained from the PC and EC processes.

The evaluation of H_2 production and the removal of TZ and TC involved sampling at 60-minute intervals over 240 minutes. The absorbance of the samples was quantified using a UV-Vis spectrophotometer at a wavelength of 427 nm and 277 nm for TZ and TC, respectively, at pH 5. The pollutant removal rate was ascertained using the established Equation 1. The method involved continuously stirring the solution while concurrently engaging the mercury lamp and the power supply.

$$\%\ Removal = \frac{C_O - C}{C_O} \times 100\% \quad (1)$$

C_O and C were the concentrations of dissolved pollutants in milligrams per liter (parts per million) during the first- and subsequent time intervals, respectively. The H_2 concentration was quantified using a Shimadzu GC-2015 gas chromatograph equipped with a Molecular Sieve 5A column. The carrier gas was argon, which had a retention duration.

3. Results and Discussions

3.1 Characterization of WO_3/g-C_3N_4/TiNTAs Nanocomposite as Photocatalyst

FESEM images taken from the optimal composite results achieved using the IA method are depicted in Fig. 1. It illustrates that the integration of g-C_3N_4 and WO_3 does not affect the morphology of TiNTAs. The structure can be evaluated based on three main metrics such as outer diameter, wall thickness, and nanotube length. In pure TiNTAs, the outer diameter ranges from 165-205 nm, the wall thickness fluctuates between 20-29 nm, and the nanotube length ranges from 881-921 nm. Meanwhile, the W-CN-TiNT nanocomposite has an outer diameter range of 98-126 nm, wall thickness ranges from 18-20 nm, and nanotube length fluctuates from 1125-1153 nm. These findings indicate that the integration of g-C_3N_4 and WO_3 via the IA synthesis method does not significantly affect the morphology of TiNTAs.

The EDX element mapping based on Fig. 1 (inset bottom) shows that carbon (C), tungsten (W), and oxygen (O) components are found in TiNTAs. It indicates that the composition of melamine and Na_2WO_4 $2H_2O$ is well-doped in TiNTAs. Nitrogen (N) element is not identified at any point on the nanocomposite surface because the main factors are most likely the small nitrogen peak and low g-C_3N_4 concentration. However, the incorporation of WO_3 and g-C_3N_4 into TiNTAs does not result in particle aggregation or clumping. It is important because aggregation can reduce the catalytic activity of TiNTAs (Pratiwi *et al.*, 2025). Therefore, the structure of TiNTAs remains essentially unchanged from that of both doped materials. This study indicates that the specific nanotube structure remains stable, without aggregation, which can reduce catalytic effectiveness, and the morphology does not change significantly with the addition of WO_3 and g-C_3N_4. The results clearly suggest that the composition and synthesis used are effective in maintaining the structural integrity of TiNTAs.

Fig. 2 illustrates the HR-TEM/SAED evaluation of W-CN-TiNT nanocomposites synthesized using the IA method. The crystal structures of rutile TiO_2, anatase TiO_2, and WO_3, along with g-C_3N_4, are observed, which display interplane spacing of about 0.32 nm, 0.357 nm, 0.375 nm, and 0.326 nm. The findings reveal these interplane spacings. The mentioned interplane spacing of 0.32 nm is related to the (1 1 0) plane of rutile TiO_2 crystal form, and the mentioned spacing of 0.357 nm is related to the (1 0 1) plane of anatase TiO_2 crystal. The determined spacing of 0.375 nm is directly related to the (1 0 1) plane of the WO_3 crystal, while the spacing of 0.326 nm is related to the (0 2 0) plane of the g-C_3N_4 crystal. The data are validated by JCPDS No. 21-1272, specifically for anatase TiO_2 from JCPDS No. 00-

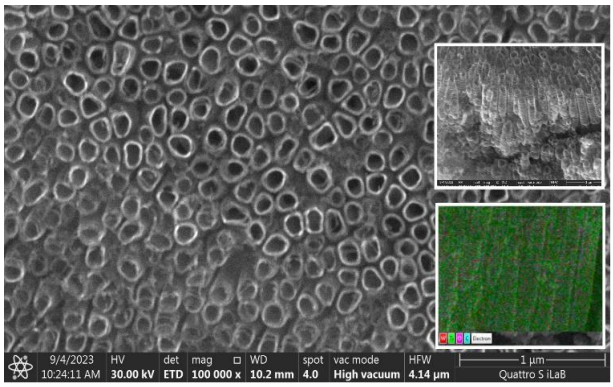

Fig. 2 FESEM Image of W-CN-TiNT (Inset Top: FESEM image from nanotube side, inset Bottom: EDX elemental mapping)

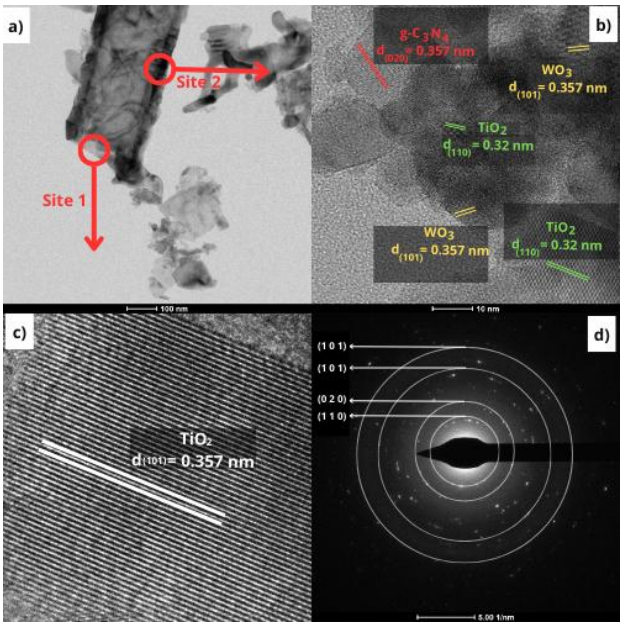

Fig. 1 a) TEM, b) & c) HR-TEM image; and d) SAED Diffraction Pattern of W-CN-TiNT.

033-1387 for WO_3. Although the concentration of g-C_3N_4 in TiNTAs is low, SAED analysis effectively detects its presence.

Additionally, TEM results uncover that the diameter of the nanotubes increase toward the base. This effect originates from the anodization process, where the higher dissolution of hexafluoro titanium ($[TiF_6]^{2-}$) species from the nanotube walls causes a larger inner diameter of the resulting nanotubes. The reaction is shown in Equations 2-4 (Muttaqin *et al.* 2022a). This poses certain difficulties for the g-C_3N_4 and WO_3 precursors. Both must penetrate the interior of the nanotubes. In conclusion, TEM, HR-TEM, and SAED characterizations indicate that the synthesis of g-C_3N_4, WO_3, and TiNTAs nanocomposites is successful.

$$2H_2O \rightarrow O_2 + 4e^- + 4H^+ \quad (2)$$

$$Ti + O_2 \rightarrow TiO_2 \quad (3)$$

$$TiO_2 + 6F^- + 4H^+ \rightarrow TiF_6^{2-} + 2H_2O \quad (4)$$

Fig. 3 shows the XRD results of W-CN-TiNT nanocomposites synthesized by the IA method. It demonstrates that the nanocomposites have various crystal phases, including anatase and rutile forms of TiO_2, g-C_3N_4, WO_3, and titanium metal. Some typical diffraction peaks of anatase TiO_2 are located at 2θ = 25.67°, 38.31°, 48.06°, 54.64°, and 55.66°, which correspond to the crystal planes (101), (103), (004), (202), and (211) according to JCPDS No. 21-1272 (Scarpelli *et al.*, 2018), respectively. It indicates that the nanocomposites have a complex crystal structure with a mixture of various phases.

The rutile phase of TiO_2 was identified at 2θ = 27.56° and 35.04°, which correspond to the (1 1 0) and (1 0 1) planes as per JCPDS No. 21-1276 (Phromma *et al.*, 2020). Specific planes, (1 0 0), (0 0 2), and (1 0 2), were identified at 2θ of 38.86°, 40.65°, and 53.49°, respectively. It denotes the presence of titanium (Moura *et al.*, 2012). g-C_3N_4 shows relatively low peaks at 2θ = 27.56° (0 0 2) and 44.81° (1 0 0) according to JCPDS No. 87 – 1526 (Karimi-Nazarabad & Gohar-shadi, 2017). This might be due to the low concentration of g-C_3N_4 dopant coupled with inadequate crystallization of melamine. WO_3 diffraction is clearly observed at 2θ = 23.28° and 36.65°. These values correspond to the (1 1 0) and (2 0 1) planes, respectively (Li et

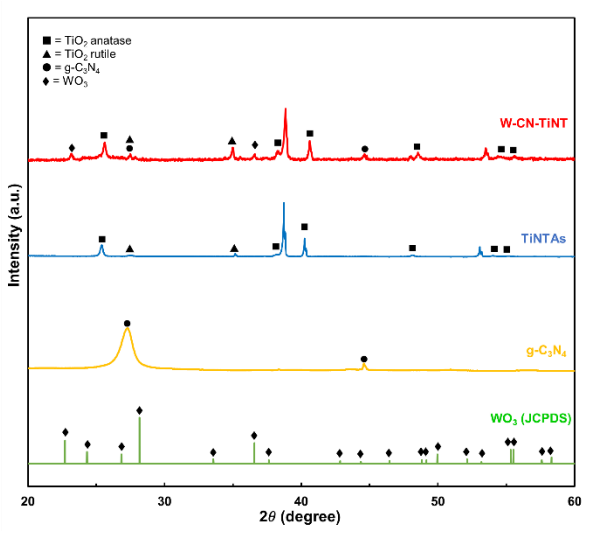

Fig. 3 XRD results of TiNTAs; g-C_3N_4; WO_3 JCPDS; and W-CN-TiNT nanocomposite

al., 2021). TiO_2 calcination at 550°C for about 3 hours with a heating rate of 3°C per minute immediately led to the appearance of the rutile phase (Husein *et al.*, 2024; Pandey *et al.*, 2020; Zhou *et al.*, 2020). This temperature optimizes the conversion of melamine to g-C_3N_4. It can also promote the formation of a rutile phase, which usually appears at temperatures above 500°C (Bamne *et al.*, 2018; Phromma *et al.*, 2020; Saalinraj & Ajithprasad, 2017). Higher temperatures increase the crystallinity of the material, which can be observed through narrower and clearer XRD peaks. The Scherrer equation is commonly used to calculate the crystallite dimensions. Anatase crystals measuring 33.14 nm are the main phase, and rutile crystals measuring 45.059 nm are the secondary phase.

The Scherrer equation provides insight into the crystallite dimensions of the synthesized nanocomposites using the IA method. This work used XRD data to measure the average crystallite size of the main diffraction peaks in the anatase and rutile crystal phases. The rutile diffraction peak appears at approximately 2θ = 27.37°, while the anatase peak is at approximately 2θ = 25.4°. The widths of these diffraction peaks are used in the Scherrer equation after determining their full width at half maximum, as described by Azizi-Toupkanloo *et al.* (2019). The anatase crystals are approximately 33.14 nm in size, while the rutile crystals are slightly larger at 45.059 nm. Analysis of the crystal phase composition suggests that the ion implantation approach favors anatase over rutile. The difference in crystallite diameter between anatase and rutile can affect the material properties, as both phases affect the characteristics in their own way. Smaller anatase crystals typically exhibit higher surface areas, thus increasing the effectiveness of photocatalysis. The fabrication conditions may have led to a gradual increase in the rutile crystal diameter, thereby helping to produce larger crystals relatively consistently, as demonstrated by Tan *et al.* (2014). Therefore, these findings provide some insights into the properties of the synthesized photocatalytic materials, particularly regarding the particle size and crystal phase composition, as confirmed by Refs. Gu *et al.* (2014), Pandey *et al.* (2020) and Zhou *et al.* (2020).

Fig. 4a illustrates the UV-Vis DRS spectra simultaneously, and Fig. 4b shows the absorbance contours of TiNTAs and W-CN-TiNT nanocomposites. The transient photocurrent spectrum is also depicted in Fig. 4c. TiNTAs have a bandgap and wavelength shown in Fig. 4a-b of 3.17 eV and 391 nm, respectively. The W-CN-TiNT nanocomposite displays a specific bandgap at 2.84 eV. In addition, the nanocomposite shows a specific wavelength at 405 nm during this period. The reduction of the bandgap in W-CN-TiNT aligns with the decrease in energy, although the wavelength remains beyond TiNTA in accordance with previous findings (Muttaqin *et al.*, 2022). This phenomenon correlates well with the mathematical expression for calculating the bandgap energy shown by Equation 5.

$$E = \frac{h.c}{\lambda} \quad (5)$$

The formula consists of band gap energy (E), Planck's constant (h), speed of light (c), and wavelength (λ). According to the estimation, the band gap of TiNTAs is 3.17 eV, which is

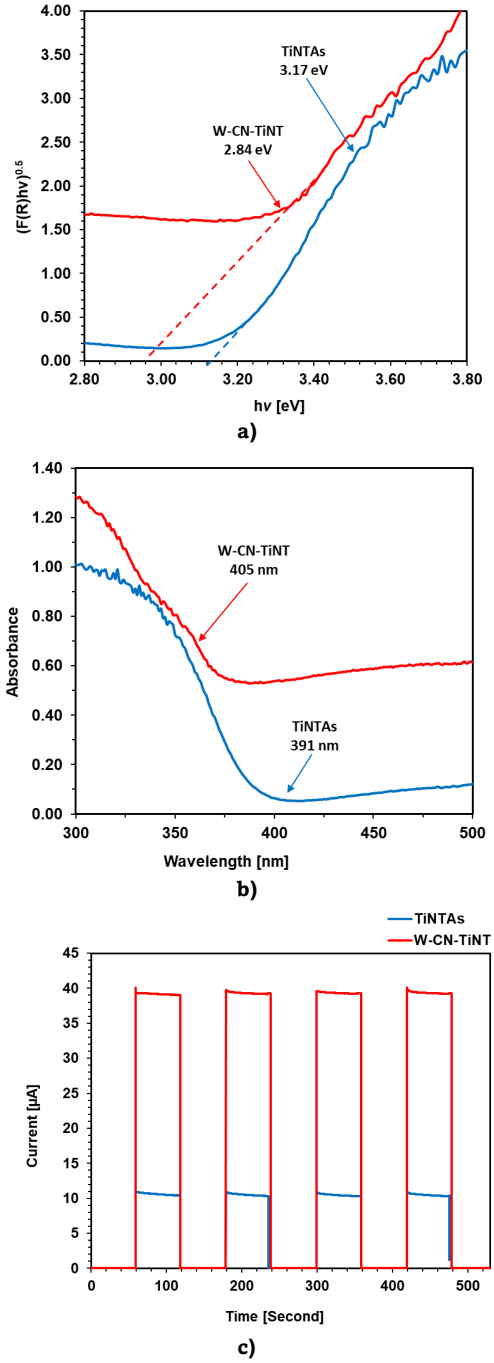

Fig. 4 Optical and photoelectrochemical behavior of W-CN-TiNT using a) UV Vis DRS Spectra; b) the absorbance shift; c) Transient Photocurrent

consistent with previous findings (Slamet and Kurniawan 2018). The incorporation of g-C_3N_4 and WO3 through cooperative strategy effectively reduces the band gap from 3.17 eV to 2.84 eV. The extension of g-C_3N_4 and WO_3 semiconductors, which have lower band gap energies, into the nanocomposite structure leads to the reduction of the band gap energy. The band gap energy of the W-CN-TiNT blend is in the range of TiNTAs, g-C_3N_4, and WO_3. This is consistent with previous judgments (Husein *et al*. 2024).

Fig. 4c shows the electron transport phenomena in pure TiNTAs and W-CN-TiNT nanocomposites under visible light irradiation. The increase of photocurrent from OFF to ON state obviously enhances the efficient charge transfer and improves the photoelectric conversion efficiency. Interestingly, the W-CN-TiNT nano-hybrids produces much higher photocurrent than most pure TiNTAs, which confirms their superiority in facilitating interfacial electron dynamics. This enhanced photocatalytic activity confirms that the W-CN-TiNT composite serves as a highly effective material for photocatalytic applications. Its superiority stems from its ability to significantly enhance the reaction kinetics, which makes it an optimal candidate for practical photochemical devices and pollution remediation technologies.

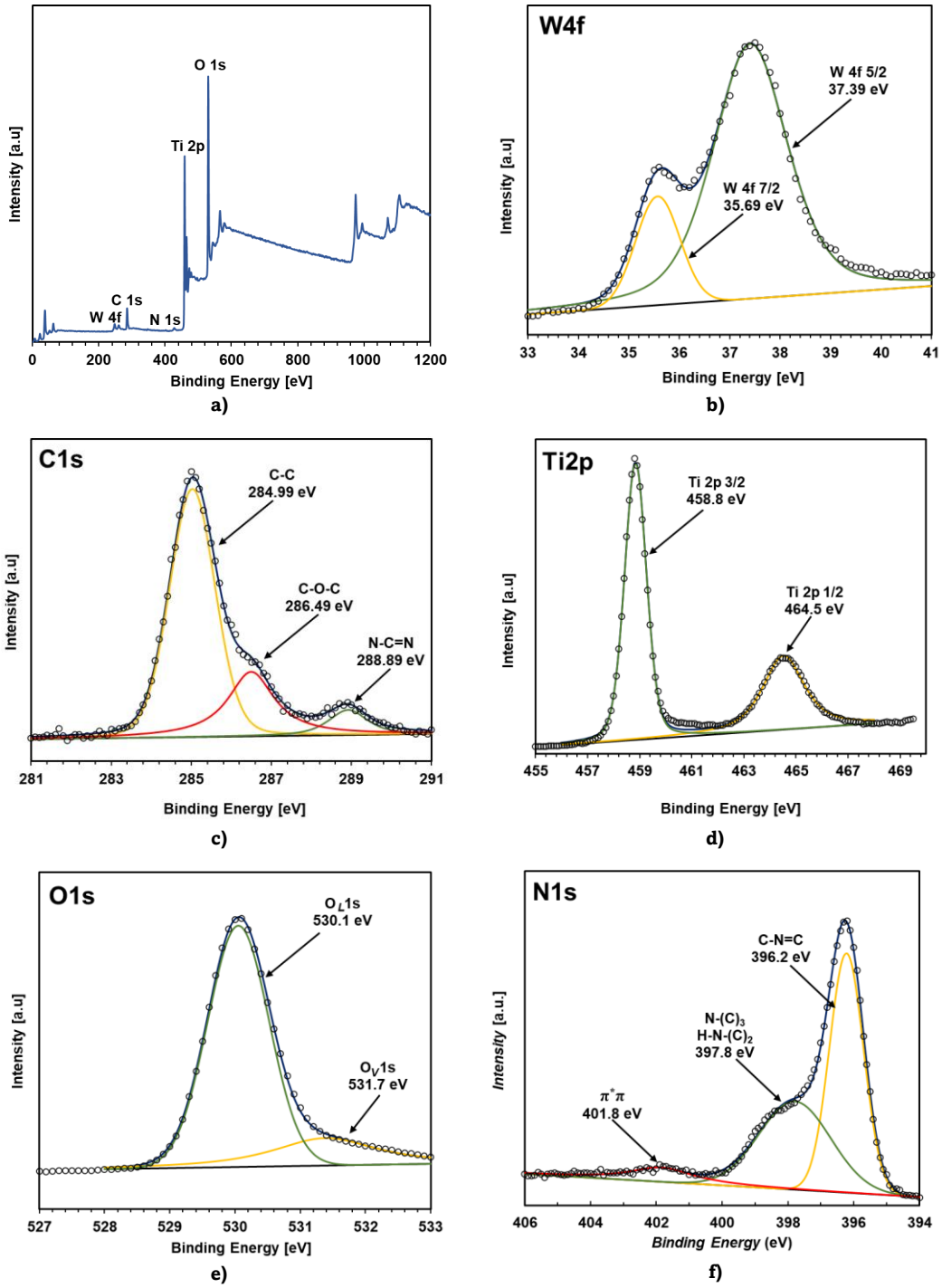

Fig. 5 Presents the XPS Spectra for a) Wide Survey, b) W 4f, c) C 1s, d) Ti 2p, e) O 1s, and f) N 1s of W-CN-TiNT.

XPS testing was performed on W-CN-TiNT nanocomposites to verify the synthesis of nanocomposites and identify the surface ions. The results, as shown in Fig. 5, indicate that the surface of the nanocomposites is composed of titanium, oxygen, tungsten, nitrogen, and carbon. Examination of the doublet peaks of the W 4f (Fig. b) component at binding energies of 35.69 eV and 37.39 eV correspond to the 4f 7/2 and 4f 5/2

orbitals of tungsten ion W^{6+}, indicating the presence of WO_3. Furthermore, a weaker peak is found to be associated with W^{5+}, indicating some oxygen deficiency in the crystal structure. The presence of multiple oxidation states of tungsten on the surface of the films, namely W^{6+} and W^{5+}, reflects the formation of W=O bonds. It helps enhance photocatalytic and electrical properties. The more prominent peaks indicate the diversity in the chemical environment around the tungsten atoms (Wang *et al*., 1998).

The C 1s spectrum reveals three important peaks in Fig. 5 c). First and foremost, the peak at 284.57 eV indicates C-C bonds, which may originate from trace impurities. Furthermore, the peak at 287.04 eV typically indicates N=C-N bonds, which implies the g-C_3N_4 architecture described by Lei *et al*. (2011). This differentiation of g-C_3N_4 peaks is due to the increased conjugation relative to standard g-C_3N_4. In addition, the Ti 2p spectrum splits into two locations (Fig. 5d) at 458.8 eV for Ti 2p 3/2 and 464.5 eV for Ti 2p 1/2 with a splitting energy of about 5.7 eV. It validates the presence of some Ti^{4+} ions in TiO_2. The lack of a peak near 455 eV distinguishes TiO_2 from metallic titanium since it requires complete oxidation of the titanium substrate (Ti^0) (Qahtan *et al*., 2024).

The O 1s spectrum (Fig. 5e) depicts two obvious peaks at 530.1 eV and 531.7 eV. The initial peak at 530.1 eV indicates the lattice oxygen (O_L) in the crystal framework of TiO_2 and WO_3. Meanwhile, the secondary peak at 531.7 eV denotes the presence of oxygen vacancies or hydroxyl groups (O_V) along the surface of the materials. These oxygen vacancies act as electron traps that enhance the photocatalytic effectiveness of the materials, respectively, as documented in various studies (Stefanov *et al*. 2008). The N 1s spectrum (Fig. 5f) exhibits three main peaks at 396.22 eV, 397.79 eV, and 401.84 eV. The peak at 396.22 eV is related to the C-N=C bond in the g-C_3N_4 heptazine structure. Meanwhile, the peak at 397.79 eV is associated with the nitrogen bonded to three carbon atoms. The peak at 401.84 eV indicates the presence of nitrogen. The smaller concentration of nitrogen atoms (ranging from 0.7 to 0.2%) provides evidence for the presence of oxidized nitrogen on the outside of the nanocomposite.

XPS examination reveals the chemical composition and oxidation states of the components inside the ternary nanocomposite. The presence of W^{6+}, W^{5+}, Ti^{4+}, and the g-C_3N_4 supports the creation of a complex photocatalytic material. Oxygen deficiency and vacancies enhance photocatalytic activity, whereas the combination of TiO_2, WO_3, and g-C_3N_4 creates a diverse and beneficial chemical environment.

3.2 Photocatalysis for Hydrogen Production and Pollutant Removal

The novel W-CN-TiNT nanocomposites synthesized using the IA method effectively produce H_2 gas and remove pollutants. After four hours of testing, the materials achieved H_2 production rates of 0.36 mol H_2/m^2 for TZ, 0.35 mol H_2/m^2 for the TZ+TC mixture, and 0.33 mol H_2/m^2 for TC, as shown in Fig. 6a. The nanocomposites could utilize light and convert it into renewable energy in the form of H_2. Furthermore, this photocatalytic approach demonstrates its effectiveness for the removal of pollutants from the environment or pharmaceutical industry processes, as depicted in inset Fig. 6b, with removal

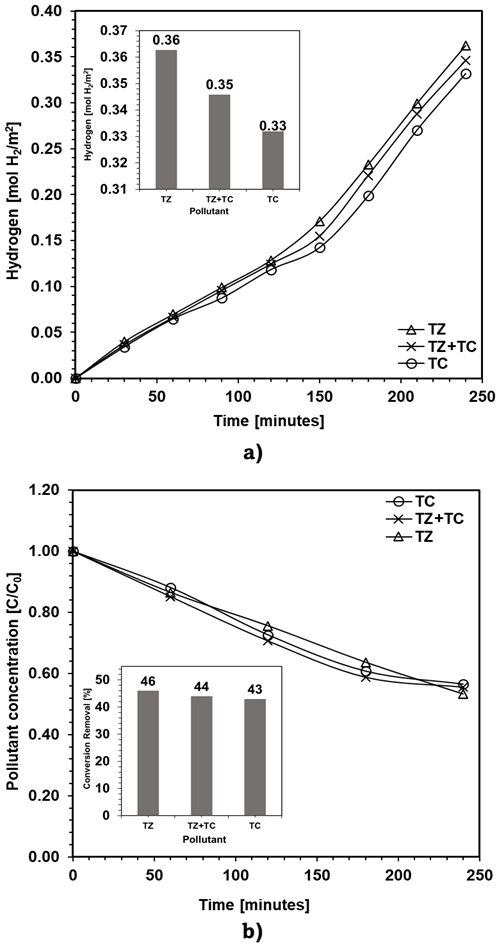

Fig. 6 Integration of the PC process performance of W-CN-TiNT in a) H_2 production and b) pollutants removal (inset 'a)' hydrogen output after 240 minutes and inset, 'b)' conversion removal after 240 minutes).

rates of 46%, 44%, and 43% for TZ, TZ+TC, and TC, respectively.

The vertical axis of the graph in Fig. 6b illustrates the ratio of the concentration at a given time (C) relative to the initial concentration (Co). It represents the amount of pollutant residue remaining over time. This C/Co value provides a measure of how much of the pollutants are removed from the system over time. If a C/Co ratio is close to one, it indicates a little reduction, while a much lower value indicates an effective pollutant removal. Fig. 6b compares the performance of W-CN-TiNT using the PC process in removing TC, TZ, and TZ+TC pollutants. In particular, it shows that the PC is the most adequate in rapidly reducing the number of pollutants, highlighting its enhanced depuration capability.

In general, based on the data shown in Figures 6a-b, the removal of TZ is easier than that of TC and TZ+TC. This pollutant also produced more H_2. The ease of TZ removal is due to its simpler structure. TZ contains several -N=N- bonds that •OH can easily break during the photocatalytic process. The simplicity of its structure allows the rapid removal of TZ. It also maintains the high effectiveness of the catalyst in facilitating the electron transfer from protons (H^+) to H_2. In contrast, TZ+TC has a very complex molecular composition that requires more energy to break it, thus slightly reducing the productivity of H_2 production and removal compared to TZ. Similarly, TC displays a more complicated chemical structure with several functional groups such as hydroxyl, amino, and carbonyl, which prolong its removal time. As a result, the relative performance of TC is

lower than that of TZ and TZ+TC in terms of H_2 production and pollutant removal efficiency. Although TZ+TC is a complex molecule, the presence of TZ in its mixture gives it a clear advantage over TC. The TZ bond, which can be easily cleaved by reactive species, accelerates the removal process. The removal percentage of TZ+TC is close to 44%. It exceeds the removal percentage for TC (43%). Therefore, photocatalytic efficacy is highly dependent on the chemical constitution of the organic compound. Compounds with relatively simple structures, such as TZ, show higher efficacy in H_2 production. Similarly, they exhibit higher efficacy in pollutant removal.

3.3 Kinetic investigations of WO_3/g-C_3N_4/TiNTAs Nanocomposite

Fig. 7 illustrates the kinetic profiles for the removal of TZ (Fig. 7a) and TC (Fig. 7b) using the highly effective W-CN-TiNT nanocomposite photocatalyst. With an expansive surface area of 0.0064 m^2, these nanomaterials interact between their abundant active sites and contaminant molecules, thereby significantly increasing the removal percentage over time. The initial concentration used in this study for TZ and TC solutions is 10 ppm. Kinetic analysis showed that TZ follows a reaction order of 1.87 with a rate constant of 3.63×10^{-5} $ppm^{0.87}$ m^2 min^{-1}, while TC corresponds to an order of 1.54 and occurs at 4.80×10^{-6} $ppm^{0.54}$ m^2 min^{-1}. The differences in these parameters suggest that different molecular architectures can significantly affect the degradation rate.

TC has stronger resistance to •OH attack and different responsive oxygen species due to its benzene ring quartet, which results in a very strong and stable aromatic structure. The extended subatomic size of TC hinders contact with the specific dynamic points of the catalyst, which then gradually breaks the molecule. In contrast, the simple benzene ring group of TZ and the weak resonance bond make it more susceptible to radical attack. The anionic nature favors Electrostatic Interaction with the dynamic space of the catalyst to accelerate the removal. The damage to the molecular structure of TZ and TC was evaluated by LC-HRMS. The LC-HRMS results revealed that TZ is removed more effectively than TC, although not significantly.

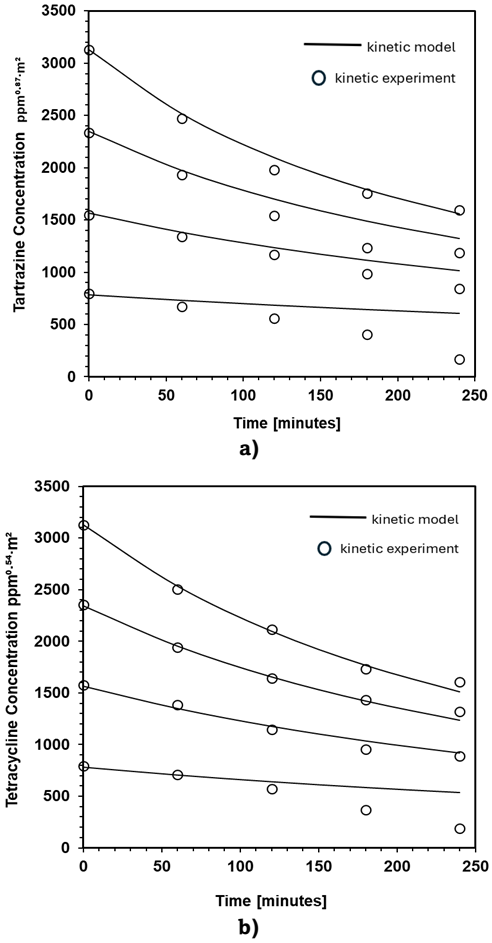

Fig. 7 Calculated parameters from kinetics studies: a) Tartrazine, b) Tetracycline.

Pollutants + •OH → Removal Product. (6)

The reaction of elimination of TZ and TC conducted via the PC process is shown in Equation 6. The primary objective of the kinetic study is frequently to enhance comprehension of the efficacy of a catalyst employed in PC. Through the examination of a singular system, researchers may ascertain surface efficiencies, pollutant reactivity, and the influence of reaction parameters on degradation rates. It includes the light intensity and initial compound concentration. Such investigations exhibit greater reproducibility and yield more consistent data compared to compound systems characterized by numerous connected factors. This mechanism entails light-induced electron excitation, chemisorption, the generation of reactive oxygen species, particularly •OH radicals, and the oxidation of organic molecules into CO_2 and H_2O (Berger *et al.* 1997; Vasudevan *et al.* 2009).

Fig. 7 demonstrates that the reaction rate is affected by the concentration of TZ and TC in a non-linear exponential form, and it depends directly on the available active surface area. In general, the model curves show good agreement with the experimental data, especially at high concentrations. However, at reaction times above 120 min, especially when the concentrations of TZ and TC are lower, there is a deviation between the experimental data and the model predictions. This is indicated by the position of the experimental data points below the curve. Further study is needed to clarify the causes of this phenomenon, as it lies beyond the scope of this discussion.

A linear model derived from a kinetic study exhibits an exceptional match with the experimental data. It is proved by a coefficient of determination (R^2) nearing 1, which signifies a robust association. The reaction rate is mostly affected by surface chemical interactions rather than diffusion constraints. It indicates that the process adhered to intrinsic kinetics. Due to the employment of a heterogeneous catalyst, the reaction order is non-elementary, rendering the constant rate unable to be determined exclusively from *k* values. Consequently, the assessment of removing performance is more accurately determined by the real reaction rate.

The findings suggest that the W-CN-TiNT nanocomposite exhibits significant potential for wastewater treatment, especially in the removal of organic pollutants like TZ and TC. This method enhances the targeting of diverse organic contaminants in industrial wastewater, hence mitigating environmental concerns.

3.4 The Mechanism of Tartrazine-Tetracycline Removal

The removed TC and TZ compounds help the environmental recovery process after the disposal of pharmaceutical and organic pollutants. This study used the LC-HRMS method to examine the elimination of both substances. By utilizing the m/z value, this approach can identify molecular fragments that are removed. The elimination mechanism in the W-CN-TiNT-based photocatalytic system involves chemical interactions with reactive oxygen species (ROS), such as superoxide (O_2^-), hydroxyl radicals (•OH), and holes (h^+), which are used as the removal of pollutant species (Vaiano *et al.*, 2016).

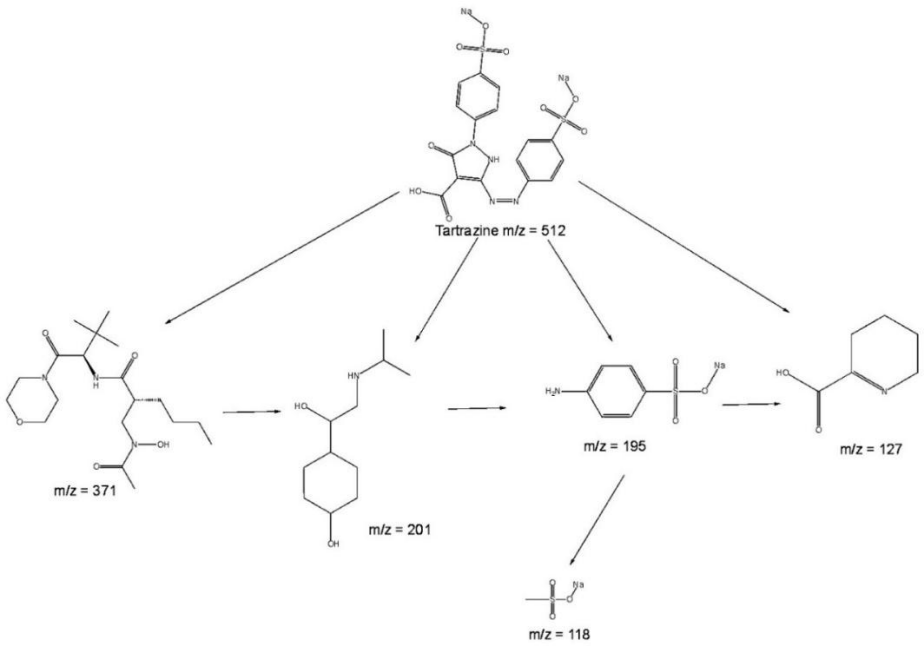

Fig. 9 Proposed TZ Removal Pathway under Photocatalytic Conditions

As can be seen in Fig. 9, the light stimulates the W-CN-TiNT photocatalyst that excites the electrons (e^-) and forms h^+. It starts with the analysis of TZ. Excited electrons react with oxygen (O_2) to produce superoxide radicals ($\bullet O_2^-$). The holes transform water molecules or hydroxide ions (OH^-) into •OH. These reactive species target the TZ structure (m/z = 512), primarily at the azo bond (-N=N-). It results in an initial fragment with m/z = 195 that comprises an amine group ($-NH_2$) and a sulfonate group ($-SO_3^-$). The $\bullet O_2^-$ and •OH engage with the bonds in the TZ molecule, causing additional cleavage. •OH attacks the aromatic ring and sulfonate moiety. •OH is a very powerful oxidizing agent. The release of the sulfonate group produced fragments with m/z = 118. The ring opens, releasing additional fragments with m/z values 371 and 201. h^+ participates in direct oxidation, which accelerates the breakdown of the aliphatic fragment with m/z 127. When these systems work together, they remove TZ to smaller, harmless metabolites.

TC (m/z = 444) is a photosensitive antibiotic despite having a stable amine group and a polyhydroxy aromatic structure (Wu *et al*., 2020). When exposed to light, the W-CN-TiNT system produces reactive oxygen species (ROS), which disrupt the chemical bonds in TC, as shown in Fig. 8. Reactive oxygen species include hydroxyl radicals and superoxide anions. When C-C or C-N bonds split, a fragment with m/z = 425 is formed, continuing the fragmentation process. The next step is to cleave or decarboxylate the side chain, yielding a fragment with a mass of 382 moles. The m/z value of 332 suggests that the TC core structure has been removed because of increased component fragmentation. The m/z = 320 fragments represent the removal of the aromatic ring, resulting in a linear or cyclic structure.

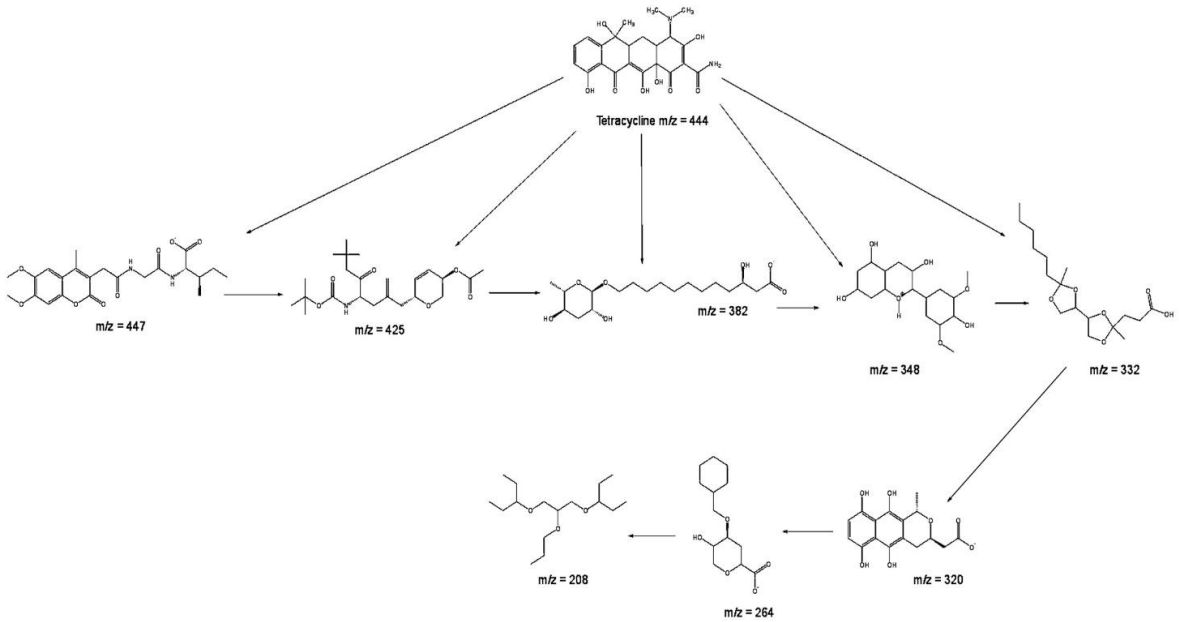

Fig. 8 Proposed TC Removal Pathway under Photocatalytic Conditions

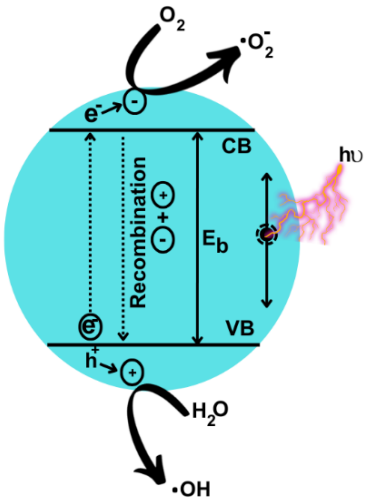

Fig. 11 Illustration of PC (Hoffmann et al., 1995). Semiconductors in photocatalysis absorb sufficient energy (hv > Eb), which activates the photocatalyst and produces electron-hole pairs ($h_{vb}^{+}-e_{cb}^{-}$). The interaction of electrons and holes with oxygen and the surrounding air causes the formation of reactive oxygen species (ROS), such as $\bullet O_2^-$ and •OH. The combination of positive and negative charges can occur rapidly on the surface or inside the photocatalytic material if the electron-hole pairs fail to migrate.

Finally, the fragment with m/z = 208 indicates that TC has been entirely removed into a non-toxic, inert compound.

The unique W-CN-TiNT photocatalyst has remarkable properties that facilitate the removal of organic pollutants. As depicted in Fig. 10, the surface area of the material is very large and effectively absorbs light across the UV-visible spectrum. It allows for interactions between target molecules and reactive oxygen species. The results of the LC-HRMS study indicate that this catalyst could efficiently convert TZ and TC into non-toxic and simpler metabolites. The application of this catalyst can serve as a useful way to improve pharmaceutical and industrial pollutants streams while helping in overall global environmental protection. When combining TZ and TC, the W-CN-TiNT photocatalyst has shown the ability to decompose them into small and non-toxic particles. Reactive oxygen species such as hydroxyl radicals and molecular oxygen initiate the removal process by breaking molecular bonds. As revealed by the LC-HRMS analysis, this photocatalyst appeared to accelerate the decomposition of hazardous pollutants dramatically. This suggests that this material can be used to manage pharmaceutical and industrial pollutants in an environmentally friendly manner.

3.5 Tartrazine-Tetracycline Removal via Electrocoagulation

This study used aluminum (Al) plates as the anode and stainless steel as the cathode for EC. Aluminum was selected because of its ability to generate Al^{3+} ions during electrolysis. It interacted with pollutants in the solution to create flocs that can be readily removed from the water. Stainless steel serves as the cathode due to its excellent corrosion resistance and mechanical stability. This procedure employed NaCl electrolyte at a concentration of 0.2 g/L to augment the conductivity of the solution and optimize the efficacy of EC. The EC process capability is shown to be proportional to the quantity of electrical energy consumed by Eqs.7-10 (Mollah *et al.* 2001). The reactions that occur during the EC process are outlined below:

Reaction at cathode (reduction):

$$2H_2O + 2e^- \rightarrow H_2 + OH^- \quad (7)$$
$$2H^+ + 2e^- \rightarrow H_2 \quad (8)$$

Reaction at anode (oxidation):

$$Al \rightarrow Al^{3+} + 3e^- \quad (9)$$
$$2H_2O \rightarrow O_2 + 4H^+ + 4e^- \quad (10)$$

In bulk solution:

$$Al^{3+} + 3H_2O \rightarrow Al(OH)_3 + 3H^+ \quad (11)$$

The experimental findings, as shown in Fig. 10, indicate that the efficacy of EC in pollutant removal is contingent upon the sample type. According to Fig. 10a, the TZ sample generates the maximum H_2 at 161 mol H_2/m^2, TZ+TC at 158 mol H_2/m^2, and TC at 145 mol H_2/m^2. The trend of rising H_2 production over time demonstrates that the electrochemical reaction aids in pollutant removal while facilitating H_2 gas production via the reduction of H^+ ions at the stainless-steel cathode. According to Fig. 10b, the TZ sample exhibits the highest removal rate at 94%, followed by the TZ+TC at 89% and TC at 80%. This suggests that EC is superior in eliminating TZ compounds compared to the TZ+TC mixture or pure TC.

The disparity may result from the chemical characteristics of each substance, which influence their interaction with Al^{3+} ions. Moreover, the generation of H_2 gas during EC exhibits notable variations. The EC process entails the oxidation of the aluminum anode, that is resulting in the generation of Al^{3+} ions (Brinzila *et al.* 2014; Rahmati, Nayebi, and Ayati 2021). The ions interact with hydroxide (OH^-) in the solution. Consequently, it

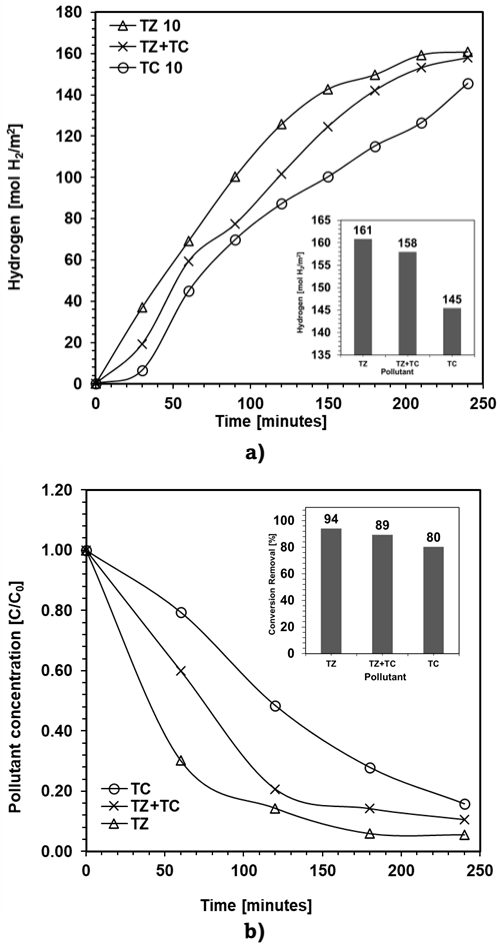

Fig. 10 Integration of the EC process performance of W-CN-TiNT in a) H_2 production and b) pollutants removal (inset 'a)' hydrogen output after 240 minutes and inset 'b)' conversion removal after 240 minutes).

Table 1
Summary of materials, synthesis method, and processes for pollutant removal and hydrogen production

No.	Ref.	Materials	Method	Process	Pollutants		H_2 Production
					Types	Elimination	
1	Ates *et al.*, 2016	ZnO, TiO_2	Hydrotermal	PC, EC, dan EC-PC	Phenol and dye compounds	88% (ZnO), and 100% (TiO_2)	
2	Li *et al* 2020	CdS and MnS	CVD	PC, EC	Rhodamine B	22.60%	1.595 mmol h^{-1} g^{-1}
3	Zakir *et al.*, 2022	Ag-Cu-doped TiO_2 nanotubes	IA	PC	*Methyl Red*	92.61%	
4	Slamet *et al.*, 2022	CuO-TiO_2 Nanotube Arrays	SILAR	PC, EC, dan EC-PC	TZ	80%	1.84 mmol.m^{-2}
5	Muttaqin *et al.*, 2022	Fe-TiNTAs	SILAR	PC, EC, dan EC-PC	MB and ciprofloxacin (CIP)	100% (MB) and 90% (CIP)	393 mmol.m^{-2}
6	Pratiwi *et al* 2023	CdS/TiO_2 *Nanotube Arrays*	SILAR	PC	CIP	45%	0.191 mmol.m^{-2}
7	Kustiningsih *et al.*,2023	TiO_2 Nanotubes	Anodization process	PC-EC	*Methyl Blue*	59.66%	
8	Suharjo *et al.*, 2024	CuO-TiO2 Nanotube Arrays	SILAR	PC-EC	E.Coli	99.90%	
9	Pratiwi *et al* 2025	CdS/TiO_2 *Nanotube Arrays*	PAD, SILAR	PC, EC, dan EC-PC	CIP	90% (CIP)	1.37 mmol.m^{-2}
10	This study	WO_3/g-C_3N_4/TiNTAs	IA	PC, EC, dan EC-PC	TZ, TC, TZ-TC	94% (EC and EC-PC)	237.11 mol.m^{-2}

forms the coagulant $Al(OH)_3$, as shown in Eq.12, which contributes to the adsorption of contaminants. The reduction reaction at the cathode concurrently generates H_2 gas that facilitates the ascent of the floc to the solution's surface via the flotation process. The generated floc enhances the separation of pollutants from water, thereby increasing the success of the process. The incorporation of NaCl electrolyte at 0.2 g/L augments the electrical conductivity of the solution, hence expediting electrochemical processes and improving the efficacy of EC.

$$Al(OH)_{3(s)} + Pollutants \rightarrow Al(OH)_{3(s)} \cdot Pollutants \quad (12)$$

The effectiveness of EC has been demonstrated to improve with an increase in voltage up to 5 V, hence increasing the H_2 production and pollutants removal efficiency. EC employing aluminum anodes and stainless-steel cathodes is an efficient method for pollutant removal and H_2 production, as stated in Eqs.7-11. The efficacy of this process is determined by the electrochemical properties of the electrode, the attributes of the substance being processed, and the incorporation of NaCl electrolyte, which improves the solution's conductivity (Demirci, Pekel, and Alpbaz 2015). Consequently, EC has a function as both an effective pollutant treatment method and a sustainable energy process for H_2 production (Barrera-Díaz, Lugo-Lugo, and Bilyeu 2012).

The summary data in Table 1 shows that the current study (row 4) exhibits a significant improvement in the PC, EC, and combined PC-EC processes in the removal of TZ and TC pollutants and the simultaneous production of H_2. This study achieves a high pollutant removal efficiency of 94%, and it covers the combination of TZ and TC in all pollutant categories. This performance matches or exceeds most of the previous studies. For example, according to rows 1 and 2 (Slamet *et al.* 2022), the study demonstrates a TZ removal efficiency of up to 80% using the PC-EC method, but this study only handled one type of pollutant. Similarly, rows 6 (Hou *et al.* 2016) and 9 (Muttaqin *et al.* 2022b) show higher removal efficiencies for certain dyes and pharmaceuticals, but both show the constraints for the desired overall.

Furthermore, the current study goes beyond prior work in H_2 production ability that reaches up to 2371.1 mmol m^{-2}. It is above earlier studies, such as in row 2 (Li, Liu, and Zhang 2020) at 1.595 mmol g^{-1} and row 9 at 3.31 mmol m^{-2}. The photocatalyst exhibits dual functionality in total, such as ecological remediation as well as sustainable energy generation, including H_2 production. The incorporation of W-CN-TiNT nanostructures via the IA method shows an increase in surface area, electron mobility, and visible light absorption. It provides a functional platform that can exceed previous simpler materials like ZnO (Ates *et al.* 2016) and CdS (Pratiwi *et al.* 2025).

In conclusion, the current study marks a substantial improvement in terms of pollutant versatility, removal efficiency, and H_2 production, and it corresponds to its high potential for integrated wastewater treatment and green energy applications.

3.6 Evaluating the Enhanced Performance of Photocatalysis-Electrocoagulation Integration

This study emphasizes the PC-EC integration process for removing organic pollutants and producing H_2. This approach combines PC and EC with W-CN-TiNT nanoparticles synthesized via the IA method using aluminum as the anode and stainless steel as the cathode. The pollutants contained 10 ppm of TZ, TC, and TZ+TC. The PC-EC integration approach relies on the interaction of two fundamental phenomena. EC oxidizes aluminum and produces $Al(OH)_3$. The chemical promotes the sequestration and precipitation of pollutants in water. During PC, the W-CN-TiNT nanomaterial absorbs light and generates electron-hole pairs, which cause redox reactions. This process accelerates the decomposition of organic pollutants in waste and promotes H_2 production by reducing H_2 ions (H^+) at the cathode.

The results based on Fig. 13 indicate that TZ is removed more efficiently than TC in a single procedure for pollutant removal and H_2 production. TC has a more complex structure with functional groups that are more difficult to disassemble. It makes the TC more difficult to remove just through the PC. In contrast, TZ has an azo structure (-N=N-) that makes it more sensitive to •OH destruction. Nonetheless, the results of the PC-

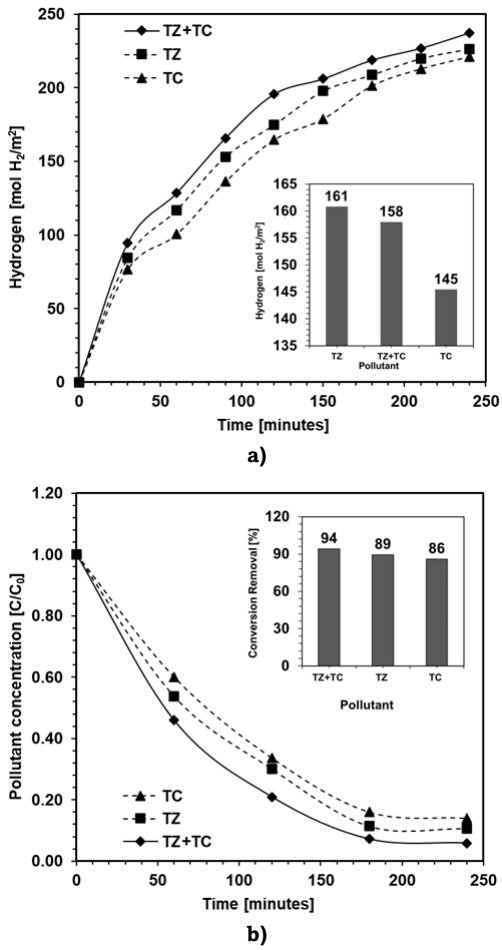

Fig. 13 Combination of PC-EC process performance using W-CN-TiNT in a) H_2 production and b) Pollutants removal (inset 'a)' H_2 output after 240 minutes and inset 'b)' conversion removal after 240 minutes).

EC Integration method show that combining pollutants TZ and TC produced the most H_2 and reduced pollutants. This effect is caused by synergistic interaction between the two types of pollutants. In PC, TZ acts as an electron donor that facilitates the increase of electron excitation. In EC, the combination of TZ and TC promotes the formation of more stable flocs, hence increasing pollutant removal efficacy. This combined strategy significantly increases H_2 production. Compared to TZ (227 mol H_2/m^2) and TC (221 mol H_2/m^2), the TZ+TC combination produced the most H_2 (237 mol H_2/m^2). This demonstrates that the redox reaction may be more efficient in the presence of mixed pollutants since it can convert a greater number of H_2 ions into H_2 gas. Furthermore, the TZ+TC combination has the highest pollutant removal efficiency of 94%, with TZ and TC reaching efficiencies of 89% and 86%, respectively. The results imply that combining PC and EC procedures is more effective at breaking down organic pollutants in water than using either process alone.

Compared to conventional H_2 production methods such as water electrolysis or methane steam reforming, the integrated EC-PC process using W-CN-TiNT offers dual benefits by simultaneously removing complex pollutants and H_2 production. While water electrolysis can produce H_2 with efficiencies exceeding 80%, it often requires high energy input and the use of pure water (Domga *et al.* 2017). The amount of H_2 produced from the steam methane reforming (SMR) process only reaches about 76% mol of the effluent gas from the

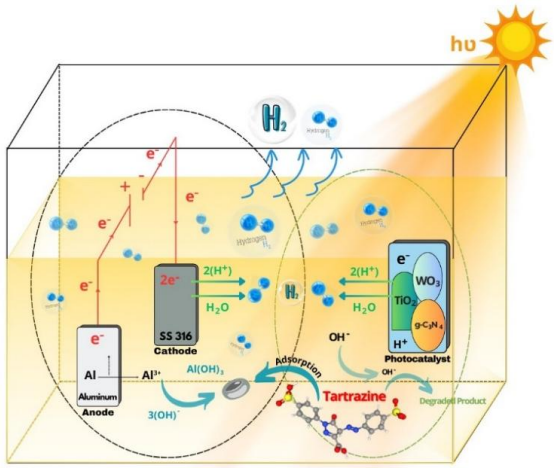

Fig. 12 Illustration of integrated PC-EC process

reformer (Barelli *et al.* 2008). Additionally, in some experiments, hydrogen concentrations can reach as high as 98–99 vol%, but this typically requires several operational cycles (Kadam, Sutar, and Yadav 2025). In contrast, this study achieves a peak hydrogen production of 237 mol/m² using industrial-like wastewater, making it a more sustainable and cost-effective alternative.

Furthermore, traditional wastewater treatment methods, such as activated sludge or membrane bioreactors, are generally less effective against emerging contaminants like TC and TZ, especially at low concentrations. The maximum degradation achieved by lignin peroxidase immobilized on various materials ranges from 70% to 95%, but this also requires multiple process cycles (Sengupta *et al.*, 2022). In contrast, the W-CN-TiNT synthesized via IA and utilized in the integrated EC-PC process not only demonstrates higher removal efficiencies (up to 94%) but also enables the valorization of pollutants into clean energy.

Fig. 12 illustrates the PC-EC process, and the reactions that occurred in the process are shown in Eqs.7-11. When the reaction continues while H_2 is liberated from the solution, the equilibrium is changed. The equilibrium shifts principle states that the release of H_2 near the solution's surface improves reaction efficiency, which then affects other reactions. The optimal outcomes in this integrated process result from H_2 liberation and the interaction of EC and PC. This combination provides various advantages to do each treatment separately. It achieves higher dye removal efficiency, lowers dye concentrations to meet pollutant quality standards more quickly, and produces less sludge than EC alone. PC converts some OH ions into OH radicals and reduces the amount of OH ions available to react with Al^{3+} ions and create $Al(OH)_3$ coagulants.

The integration of the PC-EC process offers a synergistic approach for treating complex pollutants and H_2 production simultaneously. While EC typically removes dyes and organic pollutants primarily through adsorption, and the PC enhances pollutant removal through light-activated oxidation. The combined PC-EC has demonstrated significant potential for improving both contaminant removal and H_2 production. The use of unique photocatalytic materials, such as W-CN-TiNT, further elevates the system's efficiency, enabling the effective treatment of wastewater containing persistent pharmaceutical compounds and complex organic pollutants. It presents a more sustainable and environmentally responsible alternative to conventional methods.

Considering the practical implications, the W-CN-TiNT in the integrated EC-PC process is not only superior in removing complex pollutants but also enables the valorization of pollutant streams into clean hydrogen fuel. Its application is particularly suited to decentralized treatment scenarios, including pharmaceutical manufacturing zones, hospital wastewater management, and remote or off-grid communities where wastewater treatment and renewable energy production are equally critical. Operating at a moderate voltage of just 5V and utilizing visible light, the system demonstrates low energy requirements. Moreover, the scalable in-situ anodization method used to synthesize the W-CN-TiNT photocatalyst suggests readiness for pilot-scale deployment.

Nevertheless, this study has some suggestions for further study, such as the need to identify and analyze the type of heterojunction further. Determining the type of heterojunction (Type I, II, or Z scheme) formed in W-CN-TiNT nanocomposites through additional characterization is essential. In addition, optimizing the composition ratio of W-CN-TiNT is necessary to control the formation of heterojunctions and improve the performance of the material in certain applications.

4. Conclusion

This study discloses that the PC-EC process outperforms separate processes for increasing H_2 production and removing organic pollutants. The PC approach achieves 46% pollutant removal efficiency and a maximum H_2 production of 0.36 mol H_2/m^2 (TZ). Electrocoagulation pollutants removal reaches 94% efficiency with a peak H_2 production of 161 mol H_2/m^2. The TZ+TC pollutants mixture produce the most H_2 with a maximum of 237 mol H_2/m^2. The pollutant disposal efficiency is 94%, exceeding that of the single process. The findings of this study denote that the integrated strategy is more effective at increasing H_2 production efficiency and decreasing organic pollutants. As a result, it has the potential for use in industrial wastewater treatment in a more sustainable and environmentally responsible manner.

Acknowledgments

Program Hibah Publikasi Terindeks Internasional (PUTI) Pascasarjana provided funding for this study. In addition, the authors would like to express their gratitude to the Department of Chemical Engineering, Faculty of Engineering, University of Indonesia (FTUI) for providing research facilities during the doctoral program and to the Integrated Laboratory and Research Center of the University of Indonesia (ILRC UI) for facilitating the characterization of nanocomposites. The authors also extend their appreciation to the Badan Riset Inovasi Nasional (BRIN) for the Degree by Research (DBR) scholarship and the Research Assistant program, which facilitated the first author's completion of the Doctoral program in Chemical Engineering.

Author Contributions: S.H.: Writing review and editing, conceptualization, methodology, formal analysis, writing original draft, A.H.B.; Resources, validation, analysis, supervision, E.L.D.; Supervision, analysis, discussion, validation, S.; Supervision, analysis, discussion, validation, project administration. All authors have read and agreed to the published version of the manuscript.

Funding: This study is financially supported by Program Hibah Publikasi Terindeks Internasional (PUTI) Pascasarjana, and the Contract Number is NKB-125/UN2.RST/HKP.05.00/2024.

Conflicts of Interest: The authors affirm that there are no conflicts of interest associated with the publication of this paper. The design, execution, or conclusions have not been influenced by any of the funding and support that has been received.

References

Azizi-Toupkanloo, H., Karimi-Nazarabad, M., Shakeri, M., & Eftekhari, M. (2019). Photocatalytic mineralization of hard-degradable morphine by visible light-driven Ag@g-C_3N_4 nanostructures. *Environmental Science and Pollution Research*, 26(30), 30941–30953. https://doi.org/10.1007/s11356-019-06274-9

Bamne, J., Taiwade, K., Sharma, P. K., & Haque, F. Z. (2018). Effect of calcination temperature on the growth of TiO_2 nanoparticle prepared via sol-gel method using triton X-100 as surfactant. *AIP Conf. Proc.* 2039, 020076 (2018) 020076. https://doi.org/10.1063/1.5079035

Barrera-Díaz, C. E., Lugo-Lugo, V., & Bilyeu, B. (2012). A review of chemical, electrochemical and biological methods for aqueous Cr(VI) reduction. *Journal of Hazardous Materials,* 223–224, 1–12. https://doi.org/10.1016/j.jhazmat.2012.04.054

Berge, S. M., Henderson, N. L., & Frank, M. J. (1983). Kinetics and Mechanism of Degradation of Cefotaxime Sodium in Aqueous Solution. *Journal of Pharmaceutical Sciences*, 72(1), 59–63. https://doi.org/10.1002/jps.2600720114

Bhamare, V. S. (2022). Mechanistic insight into photocatalytic degradation of antibiotic cefadroxil by 5% barium/zinc oxide nanocomposite during water treatment. *Emergent Materials*, 5(2), 413–429. https://doi.org/10.1007/s42247-021-00243-0

Brinzila, C. I., Monteiro, N., Pacheco, M. J., Ciríaco, L., Siminiceanu, I., & Lopes, A. (2014). Degradation of tetracycline at a boron-doped diamond anode: influence of initial pH, applied current intensity and electrolyte. *Environmental Science and Pollution Research*, 21(14), 8457–8465. https://doi.org/10.1007/s11356-014-2778-y

Demirci, Y., Pekel, L. C., & Alpbaz, M. (2015). Investigation of Different Electrode Connections in Electrocoagulation of Textile Wastewater Treatment. *International Journal of Electrochemical Science,* 10(3), 2685–2693. https://doi.org/10.1016/S1452-3981(23)04877-0

Di Silvestre, M. L., Favuzza, S., Riva Sanseverino, E., & Zizzo, G. (2018). How Decarbonization, Digitalization and Decentralization are changing key power infrastructures. *Renewable and Sustainable Energy Reviews*, 93, 483–498. https://doi.org/10.1016/j.rser.2018.05.068

Eidsvåg, H., Bentouba, S., Vajeeston, P., Yohi, S., & Velauthapillai, D. (2021). TiO_2 as a Photocatalyst for Water Splitting An Experimental and Theoretical Review. *Molecules*, 26(6), 1687. https://doi.org/10.3390/molecules26061687

Emamjomeh, Mohammad. M., & Sivakumar, Muttucumaru. (2009). Review of pollutants removed by electrocoagulation and electrocoagulation/flotation processes. *Journal of Environmental Management*, 90(5), 1663–1679. https://doi.org/10.1016/j.jenvman.2008.12.011

Gu, L., Wang, J., Zou, Z., & Han, X. (2014). Graphitic-C_3N_4-hybridized TiO_2 nanosheets with reactive facets to enhance the UV and visible-light photocatalytic activity. *Journal of Hazardous Materials,* 268, 216–223. https://doi.org/10.1016/j.jhazmat.2014.01.021

Husein, S., Nanda Ayu Saputri, N., Maria Ulfa, A., Studi Farmasi, P., Ilmu Kesehatan, F., Malahayati, U., & Author, C. (2023). Uji toksisitas akut limbah antibiotik streptomicyn dan tetrasiklin hcl terhadap ikan mas (Cyprinus carpio L.). *Indonesian Nursing Journal of Education and Clinic*, 3(4).

Husein, S., Rustamadji, R. R., Pratiwi, R., Dewi, E. L., & Slamet. (2024). Simultaneous tartrazine-tetracycline removal and hydrogen production in the hybrid electrocoagulation-photocatalytic process using g-C_3N_4/TiNTAs. *Communications in Science and Technology*, 9(1), 46–56. https://doi.org/10.21924/cst.9.1.2024.1308

Ji, S., Yang, Y., Zhou, Z., Li, X., & Liu, Y. (2021). Photocatalysis-Fenton of Fe-doped g-C_3N_4 catalyst and its excellent degradation performance towards RhB. *Journal of Water Process Engineering,* 40, 101804. https://doi.org/10.1016/j.jwpe.2020.101804

Jiang, Z., Zhang, W., Jin, L., Yang, X., Xu, F., Zhu, J., & Huang, W. (2007). Direct XPS Evidence for Charge Transfer from a Reduced Rutile TiO_2 (110) Surface to Au Clusters. *The Journal of Physical Chemistry C*, 111(33), 12434–12439. https://doi.org/10.1021/jp073446b

Kabdaşlı, I., Arslan-Alaton, I., Ölmez-Hancı, T., & Tünay, O. (2012). Electrocoagulation applications for industrial wastewaters: a critical review. *Environmental Technology Reviews*, 1(1), 2–45. https://doi.org/10.1080/21622515.2012.715390

Karimi-Nazarabad, M., & Goharshadi, E. K. (2017). Highly efficient photocatalytic and photoelectrocatalytic activity of solar light driven WO_3/g-C_3N_4 nanocomposite. *Solar Energy Materials and Solar Cells*, 160, 484–493. https://doi.org/10.1016/j.solmat.2016.11.005

Katrib, A., Hemming, F., Wehrer, P., Hilaire, L., & Maire, G. (1995). The multi-surface structure and catalytic properties of partially reduced WO_3, WO_2 and WC + O_2 or W + O_2 as characterized by XPS. *Journal of Electron Spectroscopy and Related Phenomena*, 76, 195–200. https://doi.org/10.1016/0368-2048(95)02451-4\

Lei, J., Chen, Y., Shen, F., Wang, L., Liu, Y., & Zhang, J. (2015). Surface modification of TiO_2 with g-C_3N_4 for enhanced UV and visible photocatalytic activity. *Journal of Alloys and Compounds,* 631, 328–334. https://doi.org/10.1016/j.jallcom.2015.01.080

Li, H., Wu, C.-H., Liu, Y.-C., Yuan, S.-H., Chiang, Z.-X., Zhang, S., & Wu, R.-J. (2021). Mesoporous WO_3-TiO_2 heterojunction for a hydrogen gas sensor. *Sensors and Actuators B: Chemical*, 341, 130035. https://doi.org/10.1016/j.snb.2021.130035

Linares-Hernández, I., Barrera-Díaz, C., Roa-Morales, G., Bilyeu, B., & Ureña-Núñez, F. (2009). Influence of the anodic material on electrocoagulation performance. *Chemical Engineering Journal*, 148(1), 97–105. https://doi.org/10.1016/j.cej.2008.08.007

Lu, X., Wang, Q., & Cui, D. (2010). Preparation and Photocatalytic Properties of g-C_3N_4/TiO_2 Hybrid Composite. *Journal of Materials Science & Technology*, 26(10), 925–930. https://doi.org/10.1016/S1005-0302(10)60149-1

Mollah, M. Y. A., Schennach, R., Parga, J. R., & Cocke, D. L. (2001). Electrocoagulation (EC) — science and applications. *Journal of Hazardous Materials*, 84(1), 29–41. https://doi.org/10.1016/S0304-3894(01)00176-5

Morozzi, P., Ballarin, B., Arcozzi, S., Brattich, E., Lucarelli, F., Nava, S., Gómez-Cascales, P. J., Orza, J. A. G., & Tositti, L. (2021). Ultraviolet–Visible Diffuse Reflectance Spectroscopy (UV–Vis DRS), a rapid and non-destructive analytical tool for the identification of Saharan dust events in particulate matter filters. *Atmospheric Environment*, 252, 118297. https://doi.org/10.1016/j.atmosenv.2021.118297

Moura, C., Munteanu, D., Cunha, L., Constantin, D. G., & Moura, C. (2012). The influence of oxygen flow during deposition on the structural, mechanical and tribological properties of titanium oxide magnetron sputtered thin films. In Article in *Journal of Optoelectronics and Advanced Materials* (Vol. 14, Issue 11).

Muttaqin, R., Pratiwi, R., Ratnawati, Dewi, E. L., Ibadurrohman, M., & Slamet. (2022). Degradation of methylene blue-ciprofloxacin and hydrogen production simultaneously using combination of electrocoagulation and photocatalytic process with Fe-TiNTAs. *International Journal of Hydrogen Energy*, 47(42), 18272–18284. https://doi.org/10.1016/j.ijhydene.2022.04.031

Nakata, K., & Fujishima, A. (2012). TiO_2 photocatalysis: Design and applications. *Journal of Photochemistry and Photobiology* C: Photochemistry Reviews, 13(3), 169–189. https://doi.org/10.1016/j.jphotochemrev.2012.06.001

Ouaissa, Y. A., Chabani, M., Amrane, A., & Bensmaili, A. (2014). Removal of tetracycline by electrocoagulation: Kinetic and isotherm modeling through adsorption. *Journal of Environmental Chemical Engineering*, 2(1), 177–184. https://doi.org/10.1016/j.jece.2013.12.009

Pandey, B., Rani, S., & Roy, S. C. (2020). A scalable approach for functionalization of TiO_2 nanotube arrays with g-C_3N_4 for enhanced photo-electrochemical performance. *Journal of Alloys and Compounds*, 846, 155881. https://doi.org/10.1016/j.jallcom.2020.155881

Pelawi, L. F., Slamet, S., & Elysabeth, T. (2020). Combination of electrocoagulation and photocatalysis for hydrogen production and decolorization of tartrazine dyes using CuO-TiO_2 nanotubes photocatalysts. *AIP Conf. Proc.* 2223, 040001 (2020) https://doi.org/10.1063/5.0000953

Phromma, S., Wutikhun, T., Kasamechonchung, P., Eksangsri, T., & Sapcharoenkun, C. (2020). Effect of Calcination Temperature on Photocatalytic Activity of Synthesized TiO_2 Nanoparticles via Wet Ball Milling Sol-Gel Method. *Applied Sciences*, 10(3), 993. https://doi.org/10.3390/app10030993

Pratiwi, R., Ibadurrohman, M., Dewi, E. L., Ratnawati, Yudianti, R., Husein, S., & Slamet. (2025). Development of CdS/TNTA nanocomposite to improve performance of simultaneous electrocoagulation-photocatalysis process for hydrogen production and ciprofloxacin elimination. *Materials Science for Energy Technologies*, 8, 121–130. https://doi.org/10.1016/j.mset.2025.01.001

Qahtan, T. F., Owolabi, T. O., & Saleh, T. A. (2024). X-ray photoelectron spectroscopy of surface-treated TiO_2 mesoporous film by 500 eV argon ion beam. *Journal of Molecular Liquids*, 393, 123556. https://doi.org/10.1016/j.molliq.2023.123556

Rahmati, R., Nayebi, B., & Ayati, B. (2021). Investigating the effect of hydrogen peroxide as an electron acceptor in increasing the capability of slurry photocatalytic process in dye removal. *Water Science and Technology*, 83(10), 2414–2423. https://doi.org/10.2166/wst.2021.136

Ratnawati, Gunlazuardi, J., Dewi, E. L., & Slamet. (2014). Effect of $NaBF_4$ addition on the anodic synthesis of TiO_2 nanotube arrays photocatalyst for production of hydrogen from glycerol–water solution. *International Journal of Hydrogen Energy*, 39(30), 16927–16935. https://doi.org/10.1016/j.ijhydene.2014.07.178

Saalinraj, S., & Ajithprasad, K. C. (2017). Effect of Calcination Temperature on Non-linear Absorption Co-efficient of Nano Sized Titanium Dioxide (TiO_2) Synthesised by Sol-Gel Method. *Materials Today*: Proceedings, 4(2), 4372–4379. https://doi.org/10.1016/j.matpr.2017.04.008

Scarpelli, F., Mastropietro, T. F., Poerio, T., & Godbert, N. (2018). Mesoporous TiO_2 Thin Films: State of the Art. In Titanium Dioxide - Material for a Sustainable Environment. InTech. https://doi.org/10.5772/intechopen.74244

Schneider, J., Matsuoka, M., Takeuchi, M., Zhang, J., Horiuchi, Y., Anpo, M., & Bahnemann, D. W. (2014). Understanding TiO_2 Photocatalysis: Mechanisms and Materials. *Chemical Reviews*, 114(19), 9919–9986. https://doi.org/10.1021/cr5001892

Shaikh, S. F., Mane, R. S., Min, B. K., Hwang, Y. J., & Joo, O. (2016). D-sorbitol-induced phase control of TiO_2 nanoparticles and its application for dye-sensitized solar cells. *Scientific Reports*, 6(1), 20103. https://doi.org/10.1038/srep20103

Sharfan, N., Shobri, A., Anindria, F. A., Mauricio, R., Tafsili, M. A. B., & Slamet, S. (2018). Treatment of Batik Industry Waste with a Combination of Electrocoagulation and Photocatalysis. *International Journal of Technology*, 9(5), 936. https://doi.org/10.14716/ijtech.v9i5.618

Sim, L. C., Koh, K. S., Leong, K. H., Chin, Y. H., Aziz, A. A., & Saravanan, P. (2020). In situ growth of g-C_3N_4 on TiO_2 nanotube arrays: Construction of heterostructures for improved photocatalysis properties. *Journal of Environmental Chemical Engineering*, 8(1), 103611. https://doi.org/10.1016/j.jece.2019.103611

Slamet, S., & Kurniawan, R. (2018). Degradation of tartrazine and hydrogen production simultaneously with combination of photocatalysis-electrocoagulation. *AIP Conf. Proc*, 020064. https://doi.org/10.1063/1.5064350

Stefanov, P., Shipochka, M., Stefchev, P., Raicheva, Z., Lazarova, V., & Spassov, L. (2008). XPS characterization of TiO_2 layers deposited on quartz plates. *Journal of Physics: Conference Series*, 100(1), 012039. https://doi.org/10.1088/1742-6596/100/1/012039

Suárez-Escobar, A., Pataquiva-Mateus, A., & López-Vasquez, A. (2016). Electrocoagulation photocatalytic process for the treatment of lithographic wastewater. Optimization using response surface methodology (RSM) and kinetic study. *Catalysis Today*, 266, 120–125. https://doi.org/10.1016/j.cattod.2015.09.016

Tan, Y., Chen, Y., Mahimwalla, Z., Johnson, M. B., Sharma, T., Brüning, R., & Ghandi, K. (2014). Novel synthesis of rutile titanium dioxide–polypyrrole nano composites and their application in hydrogen generation. *Synthetic Metals*, 189, 77–85. https://doi.org/10.1016/j.synthmet.2013.12.025

Vaiano, V., Iervolino, G., & Sannino, D. (2016). Photocatalytic removal of tartrazine dye from aqueous samples on $LaFeO_3$/ZnO

Photocatalysts. *Chemical Engineering Transactions*, 52, 847–852. https://doi.org/10.3303/CET1652142

Wang, X. G., Jang, Y. S., Yang, N. H., Yuan, L., & Pang, S. J. (1998). XPS and XRD study of the electrochromic mechanism of WOx films. *Surface and Coatings Technology*, 99(1–2), 82–86. https://doi.org/10.1016/S0257-8972(97)00415-5

Won, J. H., Kim, M. K., Oh, H. S., & Jeong, H. M. (2023). Scalable production of visible light photocatalysts with extended nanojunctions of WO_3/g-C_3N_4 using zeta potential and phase control in sol-gel process. *Applied Surface Science*, 612. https://doi.org/10.1016/j.apsusc.2022.155838

Wu, S., Hu, H., Lin, Y., Zhang, J., & Hu, Y. H. (2020). Visible light photocatalytic degradation of tetracycline over TiO_2. *Chemical Engineering Journal*, 382, 122842. https://doi.org/10.1016/j.cej.2019.122842

Zhou, S., Liu, S., Su, K., & Jia, K. (2020). Graphite carbon nitride coupled S-doped hydrogenated TiO_2 nanotube arrays with improved photoelectrochemical performance. *Journal of Electroanalytical Chemistry*, 862, 114008. https://doi.org/10.1016/j.jelechem.2020.114008